Formation of dark excitons in monolayer transition metal dichalcogenides by a vortex beam: Optical selection rules

Omadillo Abdurazakov,* Chunqiang Li, and Yun-Pil Shim†
Department of Physics, University of Texas at El Paso, El Paso, Texas 79968, USA

(Received 26 December 2022; revised 8 September 2023; accepted 12 September 2023; published 27 September 2023)

Monolayer transition metal dichalcogenides host tightly bound excitons, which dominate their optoelectronic response even at room temperatures. Light beams are often used to study these materials with the polarization—often termed the spin angular momentum of the light—providing the mechanism for exciting excitonic states. Light beams, however, can also carry an orbital angular momentum by creating helical structures of their phase front. In this work, we consider a Laguerre-Gaussian beam possessing an orbital angular momentum in addition to the spin angular momentum to create excitons in monolayer transition metal dichalcogenides. We derive optical selection rules that govern the allowed transitions to various exciton series using symmetry arguments. Our symmetry considerations show that we can create dark excitons using these high-order optical beams opening up new avenues for creating long-lived dark excitons with the potential of exploiting them in quantum information processing and storage.

DOI: 10.1103/PhysRevB.108.125435

I. INTRODUCTION

When a photon of a certain frequency illuminates a semiconducting crystal, in response an exciton can be formed. During the process, an electron excited to the conduction band binds with its hole left in the valence band through the Coulomb interaction. Because ordinary light does not couple to the electron spin, it is conserved in the process. For the direct-band-gap semiconductors, this kind of excitation is called a bright exciton, and they are short-lived because an electron can quickly recombine with the hole emitting a photon. It is also possible for an electron to flip its spin via some nontrivial processes during the exciton formation. In contrast to the bright excitons, this kind of excitation is long-lived because the excited electron cannot radiatively recombine without flipping its spin. Therefore, it is called a dark exciton and makes a promising candidate for a solid-state qubit due to its long recombination lifetime and coherence [1,2] and has lately become an active field of research in its own right [3,4].

The family of quasi-two-dimensional (quasi-2D) semiconducting crystals called monolayer transition metal dichalcogenides (ML TMDs) can host excitons of strikingly large binding energies compared to those of traditional semiconducting crystals such as GaAs [5]. This is partly due to the weak dielectric screening and geometric confinement in quasi-2D structures. Although it is an indirect-band-gap semiconductor in bulk, when exfoliated down to a monolayer [6], a TMD crystal transitions into a direct-band-gap semiconductor [7,8]. Therefore, the optical response of these materials to light is dominated by bright exciton formation and consequent photoluminescence signal at sub-band-gap frequencies. Due to the presence of heavy transition metal atoms in ML TMDs, there is a strong (moderate) spin-orbit interaction in the valence (conduction) band. Combined with the lack of spatial inversion symmetry inside the monolayer crystal, the conduction and valence bands at the $\pm K$ momentum points (or valleys) are split into two bands each that can individually host only one type of electron spin species. These bands at the two valleys are related through the time-reversal symmetry. Consequently, the electron spin and valley degrees of freedom are locked, and each valley can be selectively addressed with circularly polarized light [9–12].

Because of its valley physics and tightly bound excitons that are manifest even at room temperatures, a ML TMD crystal is an ideal platform for hosting stable and long-lived dark excitons. However, creating and controlling dark excitons in these materials is challenging as ordinary light beams do not couple to the electron spin. Nevertheless, these dark excitons can be induced to decay via radiative means by applying very strong in-plane magnetic fields [13] or coupling to the surface plasmon polaritons [14]. Although these methods offer some pathways to access the spin-forbidden dark excitons and to control their lifetimes, they are limited to extremely high magnetic fields and extremely low temperatures. Therefore, purely optical means to access and control the dark exciton states would lead to a new practical platform for many quantum applications including quantum information technology.

The polarization of light, which is used to control individual valleys in ML TMDs, corresponds to the spin angular momentum (SAM) of light and can be transferred to matter as a mechanical torque [15]. Light has another fundamental degree of freedom called orbital angular momentum (OAM). The laser beams possessing OAM can be created with holographic phase-plates, and they were already realized decades ago [16]. They are often called vortex beams and have been

*oabdurazako@utep.edu
†yshim@utep.edu

shown to induce optical transitions that are not allowed otherwise [17] and to strongly modify optical selection rules [18]. They have been used to transfer orbital angular momentum to macroscopic particles [19], individual atoms [20], as well as electrons [21], and to create Rydberg excitons in atoms [22].

In this work, we theoretically investigate the possible optical transitions with a vortex beam in ML TMD systems. Specifically, we consider a Laguerre-Gaussian laser beam, a type of vortex beam, to create spin-forbidden dark excitons as well as bright excitons in ML TMD crystals. We derive optical selection rules for such transitions based on the symmetry of the ML TMD crystal structure, the spatial structure of the beams, and the exciton envelope functions. We show that, in the quadrupole coupling regime, B-type dark excitons with various envelope functions can be created selectively in each valley. As vortex beams with high OAM can be readily created in optics labs nowadays [23], this all-optical means to create dark excitons in ML TMDs should be feasible.

The outline of the paper is as follows. First, we describe our method to identify the allowed optical transition to create excitons in these materials in Sec. II, where we consider the symmetry of the electronic bands, the spatial profile of vortex beams, and exciton envelope functions in terms of the irreducible representations of the pertinent point group to which the monolayer crystal belongs. In Sec. III, we derive and discuss optical selection rules for the bright and dark excitons. And in Sec. IV, we conclude and discuss the implication of our results to future studies.

II. METHODS

In this work, we are interested in understanding the exciton formation in a monolayer TMD crystal under the excitation of a vortex beam. By using symmetry arguments regarding the crystal band structure and light beam, we identify the allowed and forbidden optical transitions from the ground state of the crystal to various exciton states when the light beam possesses both spin and orbital angular momenta. Such an analysis grants us the optical selection rules that govern the formation of bright and dark excitons in the $\pm K$ valleys of a monolayer TMD crystal. As the band-gap energy in this class of materials lies predominantly in the optical spectrum, we only consider the direct optical transition between the spin-split valence and conduction bands at the $\pm K$ points. The symmetry of the electron wave vector around these points can be derived by constructing a tight-binding band and studying its behavior under the pertinent symmetry operations that belong to the relevant symmetry group [24].

In the single electron band picture, an exciton with the $1s$ envelope function is formed through the binding of an electron excited into the conduction-band minimum and the hole left on the valence-band maximum [25]. The exciton symmetry is defined as the direct product of the irreducible representations of the exciton envelope function, the conduction band, and the valence band, namely $\Gamma_X = \Gamma_{\text{env}} \otimes \Gamma_c \otimes \Gamma_v^*$. For the optical transition from the crystal ground state to an exciton state to occur, Γ_X must contain the irreducible representation of the driving field operator $\Gamma_{\text{beam}} = \Gamma_{\text{order}} \otimes \Gamma_{\text{OAM}} \otimes \Gamma_{\text{SAM}}$. Here, Γ_{order} is the order of optical transitions. We outline the details of the light field symmetry in the Appendix.

To find the symmetry of the electronic bands at the $\pm K$ points, we can construct a tight-binding band and assign an irreducible representation to each band. The symmetry of the exciton envelope function is found from solutions of the 2D hydrogen model, and the symmetry of the driving field operator is found by representing the polarization and the spatial structure of the Laguerre-Gaussian beam in terms of the basis functions of the relevant symmetry operations of the monolayer crystal.

In the bulk form, TMDs are indirect-gap semiconductors formed by weakly interacting layers through van der Waals forces. A monolayer of TMD, however, is a direct-gap semiconductor with a hexagonal crystal structure. The side and top view of a ML TMD crystal are depicted in Figs. 1(a) and 1(b), respectively. The crystal unit cell contains one chalcogen atom and one transition metal atom. The crystal structure is invariant under certain transformation operations. They include a threefold rotation around the principal axis perpendicular to the monolayer (C_3), a reflection around the mirror plane (σ) perpendicular to the principal axis, three twofold rotations around the axes lying on the mirror plane (C_2), and the improper rotation around the principal axis followed by a mirror reflection (S_3). This set of transformation operations, which leaves a monolayer TMD crystal invariant, belongs to the D_{3h} point group.

In the reciprocal space, the first Brillouin zone of the ML TMD crystal, which is also of a hexagonal structure, has a few high-symmetry momentum points, such as Γ, K, and $-K$, as shown in Fig. 1(e). Although the electron wave function at the Γ point inherits the point group of the monolayer crystal (D_{3h}), the symmetry at $\pm K$ points is lowered to that of C_{3h} due to the band-gap opening. Therefore, we use the irreducible representations of the C_{3h} point group in our symmetry analysis of the optical transitions. Nevertheless, one could equally use the irreducible representations of the point group of the ML TMD (D_{3h}) itself and use compatibility relationships between the two groups to derive the allowed optical transitions at individual valleys [26,27].

A tight-biding wave function at these particular momentum points can be constructed from the dominant d atomic orbitals of the transition metal atoms. According to the first-principles calculations [28], the d_{z^2} atomic orbitals dominate the conduction band, whereas the $d_{x^2-y^2}$ and d_{xy} atomic orbitals dominate the valence band at $\pm K$ points. One can construct a tight-binding band by symmetrizing these orbitals with respect to the threefold rotation operator C_3^+ relevant to the monolayer crystal symmetry. Here, the plus sign indicates that the threefold rotation operator acts in the counterclockwise direction around the principal axis. Considering the spin-orbit splitting of the valence and conduction bands at these particular momentum points, we can study the behavior of the constructed bands under the symmetry operation of the relevant double-point group using Table VIII and assign corresponding irreducible representation (irrep). The schematic diagrams for the bands and their irreps at $\pm K$ points are shown in Fig. 1(f).

The Laguerre-Gaussian beams are high-order solutions to the paraxial wave equation in cylindrical coordinates. These high-order Gaussian modes exhibit more complex spatial and phase structures compared to the regular Gaussian beams.

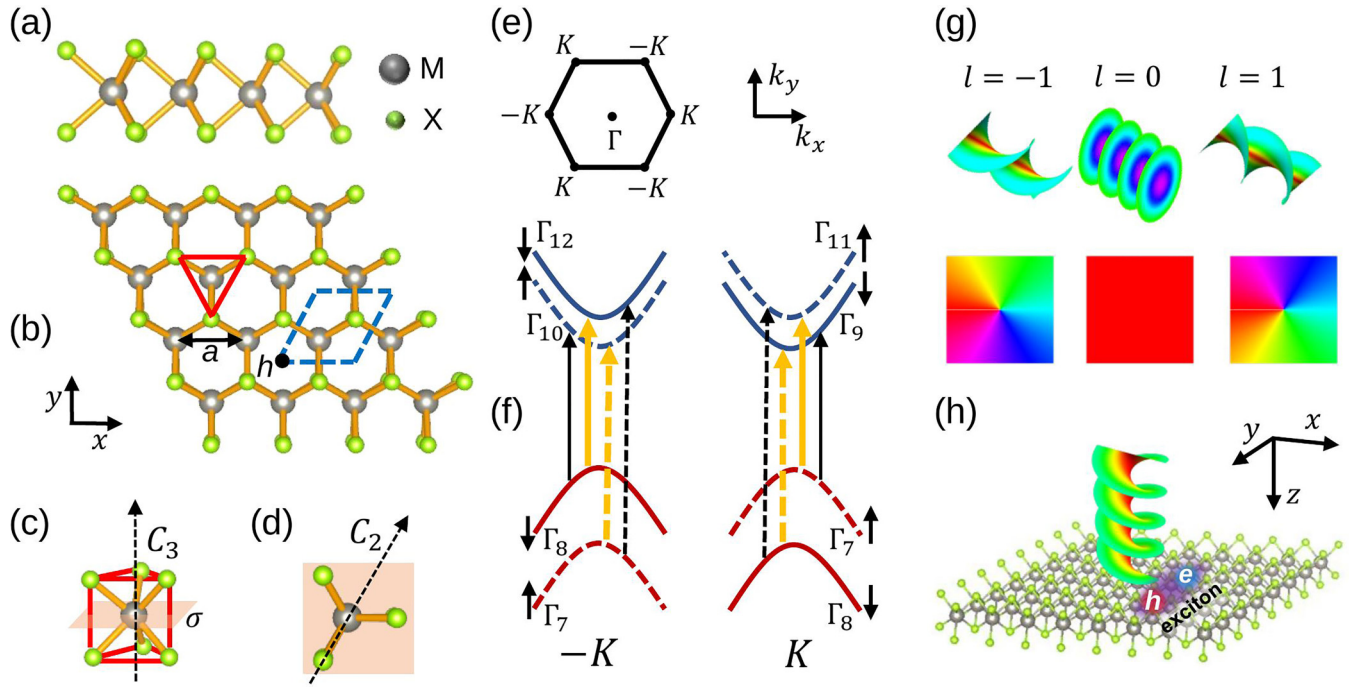

FIG. 1. Monolayer transition metal dichalcogenide (ML TMD) crystal and band structure and a vortex beam. (a) The side view and (b) top view of ML TMD crystal spanned with a unit cell (demarcated by a blue-dashed line) consisting of one transition metal and one chalcogen atom with the lattice constant of (a). (c) The principal axis with threefold rotation symmetry, a mirror plane perpendicular to this axis, and (d) three twofold rotation axes lying on the mirror plane are shown. (e) The first Brillouin zone of ML TMD and a few high-symmetry momentum points in it are shown. (f) An effective two-band model with the spin-orbit coupling splitting around K and $-K$ momentum points and the corresponding irreducible representations of the double-group relevant at the $-K/K$ points. The conduction-band splitting is exaggerated for clarity. The possible types of exciton transitions are symbolically shown by the arrows. Here, the solid (dashed) lines designate an A (B) -type exciton. The bright (dark) excitons are shown by thick yellow (thin black) lines. Note that the arrows are shifted laterally for clarity, but the transitions occur predominantly at the valley center. (g) The helical wavefront and phases of optical vortex beams are plotted for a few values of the orbital angular momentum of light. (h) Schematic of the vortex beam created exciton in a ML TMD. The vortex beam propagates along the z-axis, the direction that is perpendicular to the monolayer sample.

More importantly, due to the helical structure of their phase front, they carry orbital angular momentum along the propagation direction in addition to their spin angular momentum or polarization.

The spatial profile of the beam propagating along the z-axis in the cylindrical coordinates is given by $\boldsymbol{A}(\rho,\phi,z) = \boldsymbol{\epsilon} A_p^l(\rho,\phi,z)e^{ikz}$ [29], where

$$A_p^l(\rho,\phi,z) = C_{pl}\frac{w_0}{w(z)}\left(\frac{\sqrt{2}\rho}{w(z)}\right)^{|l|} L_p^{|l|}\left(\frac{2\rho^2}{w^2(z)}\right) \times e^{-\rho^2/w^2(z)}e^{i\Psi}e^{il\phi} \tag{1}$$

and the phase factor contains the following terms:

$$\Psi = k\rho^2/2R(z) + (2p+|l|+1)\arctan(z/z_R), \tag{2}$$

where $C_{pl} = \sqrt{2p!/\pi(|l|+p)!}$ is the normalization constant, $R(z) = z + z_R^2/z$ is the beam front curvature, and $w(z) = w_0\sqrt{1+z^2/z_R^2}$ is the spot size, which increases as a function of the distance z from the beam waist w_0. The beam acquires a nontrivial spatial structure through the associated Laguerre function $L_p^{|l|}(\rho,z)$. The intensity profile of the beam is of a ringlike structure. Its radial index p, which can be zero or any positive integer, indicates the number of rings when the beam is projected on a screen. Its azimuthal index l, which can be any integer number, indicates the amount of orbital angular momentum the beam carries. If this index is zero, a Gaussian beam with a plane-wave phase is recovered. For $p = 0$ the beam intensity has a single ring structure whose radius scales as $\propto \sqrt{|l|}$ at the beam waist. Here, $z_R = \pi w_0^2/\lambda$ is the Raleigh range, within which the beam spot size stays nearly constant. The first term in the phase factor gives a spherical curvature to the wave, whereas the latter term is called a Gouy phase, which develops as the beam propagates and mostly varies inside the Raleigh range, and λ is the wavelength of the light beam. The most significant phase term contains $l\phi + kz$. As depicted in Fig. 1(g), the points of the constant phase make a helical surface along the z-axis. For $|l| > 1$ there will be as many helices intertwined together. The center of the beam where the phase is undefined and the light intensity goes to zero is called a vortex. The lower panels in Fig. 1(g) showcase how the phase changes as a function of the azimuthal angle ϕ for corresponding values of l.

The light polarization vector $\boldsymbol{\epsilon}$ of the vortex beam depicted in Fig. 1(h) lies parallel to the two-dimensional sample and perpendicular to the beam propagation direction. Here, the beam can be either left-handed circularly polarized (σ^-) or right-handed circularly polarized (σ^+). Circular polarization of light corresponds to the spin angular momentum of light (SAM) that is directed along the longitudinal direction. A

light beam of σ^+ (σ^-) polarization carries a SAM of $+1\hbar$ ($-1\hbar$). It is also possible to employ a beam polarized along the propagation axis, and it is termed a π-polarized beam. It carries a SAM in the azimuthal direction only, and is often referred to as the transverse SAM of light [30]. One way to create a π-polarized beam is to tightly focus the vortex beam so that it is no longer in the paraxial regime and has a longitudinal component. This nonparaxial vortex beam can possess polarization that is along the beam axis that comes from the finite longitudinal field component, albeit with much weaker amplitude. This component scales as the first order in the parameter $1/(kw_0)$, which is $\sim 10^4$ times smaller than the transverse field component for a typical vortex beam spot w_0 within the optical diffraction limit [31,32]. Another method is to direct a linearly polarized Gaussian beam along the two-dimensional sample plane where its polarization is perpendicular to the sample [26]. This way, one could modify the beam-sample setup by changing the angle between them so that there is a field component perpendicular to the sample with a finite amount of π-polarization. Therefore, in this work, we also consider the possibility of having a π-polarized beam for the sake of completeness in deriving the optical selection rules.

Because of the quasi-2D structure of ML TMDs, the electric field lines between electrons and holes are screened well in the plane of the crystal and poorly screened outside. This renders the dielectric constant of the material dependent on the relative distance of the exciton envelope function. Therefore, to solve the exciton problem in ML TMD quantitatively, one needs to resort to an elaborate numerical framework such as the Bethe-Salpeter equations [33]. However, we adopt a framework that treats the exciton problem as a 2D hydrogen model with an effective dielectric screening because we are primarily interested in the symmetry properties of the exciton envelope function rather than its exact quantitative form. It was shown that one can embed the inhomogeneous screening effects into an effective dielectric constant that is averaged over the radius of an exciton and obtain a 2D analog of the hydrogenlike solutions for exciton envelope functions with quite accurate binding energies [34]. Then, the exciton envelope solutions will be of the form $\Phi_{nm}(\boldsymbol{r}) = \frac{1}{\sqrt{2\pi}} R_{n|m|}(r)\exp(im\phi)$ in real space [35,36]. The radial function R depends on the principal quantum number $n = \{1, 2, 3, \ldots\}$ and the absolute value of the magnetic quantum number $m = \{0, \pm 1, \pm 2, \ldots, \pm(n-1)\}$ with the corresponding notation of $\{1s, 2p_\pm, 3d_\pm, \ldots, (n-1)t_\pm\}$ exciton series. It also depends on the relative coordinate of the electron and hole, the exciton radius which contains the effective dielectric constant. However, we note that in the case of a ML TMD crystal, contrary to the 2D hydrogen model, the energy levels with the same n are not degenerate but differ depending on the value of n due to the nonlocal screening in 2D. As the value of n increases, the difference becomes smaller [37].

III. RESULTS

The experimental absorption measurements [8] and first-principles calculations [38] show that TMDs clearly exhibit A (B) excitons that are formed due to the direct optical transitions between the conduction band and spin-orbit split higher (lower) valence band. Here, we present the optical selection rules for bright A (B) and dark A (B) excitons created by vortex beams in a tabular form below. In addition to the usual dipole coupling, we also consider quadrupole coupling. In this work, we categorize the multipole expansions according to the order of the electric couplings. The dipole coupling regime means the electric dipole coupling, and the quadrupole coupling regime includes both the electric quadrupole and the magnetic dipole coupling terms. The quadrupole transitions become important when the electric field has a spatial gradient. Due to their complex spatial structure, high-order laser beams such as the Laguerre-Gaussian beams, especially those with high values of OAM, have a strong special field gradient. Although the oscillator strength for the quadrupole transition is much weaker than that of the dipole transition for ordinary light beams, the vortex beams can have sizable quadrupole effects that are even comparable to those of the dipole coupling at very high values of OAM because of their transverse field gradient around the center of the vortex [39,40]. Therefore, this second-order transition can no longer be ignored and needs a special consideration, especially for the vortex beams with large OAM. With the availability of the tools to create vortex beams with extremely high OAM [23], significant quadrupole exciton transition rates are plausible. To evaluate the optical transition amplitudes and dark exciton recombination lifetimes quantitatively, one needs to resort to elaborate numerical calculations such as solving the Bethe-Salpeter equations combined with the *ab initio* band-structure calculations, which will be topics of future studies. As the vortex beams carry nonzero OAM, we also derive optical selection rules for the exciton envelope functions with higher magnetic quantum numbers complementary to the $1s$ excitons.

TABLE I. Bright A and B excitons in the dipole coupling regime: Optical selection rules for *bright* excitons created by laser beams carrying orbital angular momentum (OAM) and spin angular momentum (SAM).

l (OAM)		−5	−4	−3	−2	−1	0	+1	+2	+3	+4	+5
−K	A	⊘	σ^-	σ^+	⊘	σ^-	σ^+	⊘	σ^-	σ^+	⊘	σ^-
	B	⊘	σ^-	σ^+	⊘	σ^-	σ^+	⊘	σ^-	σ^+	⊘	σ^-
K	A	σ^+	⊘	σ^-	σ^+	⊘	σ^-	σ^+	⊘	σ^-	σ^+	⊘
	B	σ^+	⊘	σ^-	σ^+	⊘	σ^-	σ^+	⊘	σ^-	σ^+	⊘

A. Bright excitons

In the single-electron picture, the bright excitons are formed when an electron and a hole of the same spins pair via the Coulomb attraction. The optical selection rules for $1s$ bright excitons in the dipole coupling regime are presented in Table I. The OAM of the vortex beam is in the range of $|l| \leqslant 5$. When the beam has no OAM ($l = 0$), the vortex beam reduces to the fundamental Gaussian beam with a circular polarization, and the well-known valley polarization optical selection rules are recovered [9]; the σ^--polarized light can only create an exciton at K valley and the σ^+-polarized light can only create an exciton at $-K$ valley. The two valleys and polarization directions are related through the time-reversal

TABLE II. Bright A and B excitons in the quadrupole coupling regime: Optical selection rules for *bright* excitons created by laser beams carrying orbital angular momentum (OAM) and spin angular momentum (SAM).

l (OAM)		−5	−4	−3	−2	−1	0	+1	+2	+3	+4	+5
−K	A	π	⊘	⊘	π	⊘	⊘	π	⊘	⊘	π	⊘
	B	π	⊘	⊘	π	⊘	⊘	π	⊘	⊘	π	⊘
K	A	⊘	π	⊘	⊘	π	⊘	⊘	π	⊘	⊘	π
	B	⊘	π	⊘	⊘	π	⊘	⊘	π	⊘	⊘	π

TABLE III. Dark A and B excitons in the dipole coupling regime: Optical selection rules for *dark* excitons created by laser beams carrying orbital angular momentum (OAM) and spin angular momentum (SAM).

l (OAM)		−5	−4	−3	−2	−1	0	+1	+2	+3	+4	+5
−K	A	⊘	⊘	π	⊘	⊘	π	⊘	⊘	π	⊘	⊘
	B	⊘	π	⊘	⊘	π	⊘	⊘	π	⊘	⊘	π
K	A	⊘	⊘	π	⊘	⊘	π	⊘	⊘	π	⊘	⊘
	B	π	⊘	⊘	π	⊘	⊘	π	⊘	⊘	π	⊘

symmetry. In this case, the same selection rules apply to both A and B excitons. When the OAM of light l is nonzero, the selection rules are modified as seen in Table I. The allowed and disallowed transitions with σ^+ (σ^-) polarization alternate for a given valley and have a periodicity of three units of the OAM of light, which is inherited from the threefold rotation symmetry of the monolayer crystal. These results for bright excitons agree well with the recent study [41] in which the authors derived similar optical selection rules for the bright 1s excitons. However, we are mainly focused on dark excitons formation in these 2D crystals. We also show the selection rules for bright excitons in the quadrupole coupling regime in Table II. We can see that we can only create excitons with particular values of l using the beams that are π-polarized, i.e., directed along the light propagation axis. However, in the paraxial wave regime, the Laguerre-Gauss beam is only polarized in the transverse direction. Therefore, no optical transitions are allowed in this regime for circularly polarized light. Nonetheless, one can employ tightly focused vortex beams that can have a polarization along the beam propagation axis [32].

B. Dark excitons

The spin-forbidden dark excitons or simply dark excitons in this work are formed when an electron and a hole with opposite spins pair via the Coulomb attraction. A light beam cannot create these states because the electric field of light does not couple to the electron spin. However, the electronic bands are made not purely of one type of spin species, but a mixture of both spin-up and spin-down species. This spin mixing is due to the spin-orbit coupling and the interaction with remote bands [26]. The conduction and valence bands, therefore, contain a dominant spin component and a smaller component for the opposite spin. The transition between these bands is decided by the symmetry properties of the bands and the light.

The optical selection rules for 1s dark excitons using vortex beams with $|l| \leqslant 5$ are presented in Table III. Here, the optical selection rules are entirely modified compared to the bright exciton cases. We can see that no circularly polarized light can excite dark excitons. Only when the beam is polarized in the direction perpendicular to the monolayer plane can one create dark excitons. For $l = 0$, only a dark A exciton can be created with the π-polarized beam that is directed parallel to the sample, which was demonstrated in photoluminescence experiments on tungsten-based TMDs [26]. However, the optical transition corresponding to the dark B exciton is categorically forbidden for any polarization direction at $l = 0$. For $|l| > 0$, dark B excitons can be excited with π-polarized light at particular values of l.

As mentioned earlier, the quadrupole transitions can be appreciable when a vortex beam is tightly focused and has a high value of OAM resulting in a strong spatial field gradient [39]. Observing that the selection rules have a fixed periodicity with respect to the values of OAM, one can easily find the allowed optical transitions at very high values of the beam OAM where the quadrupole transitions may become considerable. In Table IV, we present the selection rules resulting from the quadrupole transitions for the A- and B-type dark excitons. Both types of dark excitons can be readily created with circularly polarized light at particular values of OAM. At $l = 0$ or when the laser beam has a simple Gaussian profile, the A-type dark exciton transitions are strictly forbidden. This is the case for all values of OAM with $l \pmod 3 = 0$. With other finite OAM [$l \pmod 3 \neq 0$], A-type dark excitons can be created with circularly polarized light, but the selection rule is the same for both $+K$ and $-K$ valleys. On the other hand, the B-type dark exciton transitions are valley-dependent. For example, it is allowed with a σ^+ (σ^-) -polarized beam at the K ($-K$) valley at $l = 0$. Therefore, we can selectively create dark B excitons at a particular valley with circularly polarized light. This shows that the selection rules are manifestly altered in the presence of a nonzero OAM of light, and they differ starkly for the A and B dark excitons due to the symmetry considerations stemming from not only the band but also the spatial profile of the vortex beam, which is determined by the value of its OAM.

C. Exciton envelope functions

The experimental and theoretical studies have shown that the excitonic properties of 2D TMDs differ starkly from

TABLE IV. Dark A and B excitons in the quadrupole coupling regime: Optical selection rules for *dark* excitons created by laser beams carrying orbital angular momentum (OAM) and spin angular momentum (SAM).

l (OAM)		−5	−4	−3	−2	−1	0	+1	+2	+3	+4	+5
−K	A	σ^-	σ^+	⊘	σ^-	σ^+	⊘	σ^-	σ^+	⊘	σ^-	σ^+
	B	σ^+	⊘	σ^-	σ^+	⊘	σ^-	σ^+	⊘	σ^-	σ^+	⊘
K	A	σ^-	σ^+	⊘	σ^-	σ^+	⊘	σ^-	σ^+	⊘	σ^-	σ^+
	B	⊘	σ^-	σ^+	⊘	σ^-	σ^+	⊘	σ^-	σ^+	⊘	σ^-

TABLE V. Bright A and B excitons in the dipole coupling regime: Optical selection rules for the *bright* A and B excitons created by laser beams carrying orbital angular momentum (OAM) and spin angular momentum (SAM) for $1s$ and $2p_\pm$ exciton envelope functions.

l (OAM)		−5	−4	−3	−2	−1	0	+1	+2	+3	+4	+5
$1s$	−K	⊘	σ^-	σ^+	⊘	σ^-	σ^+	⊘	σ^-	σ^+	⊘	σ^-
	K	σ^+	⊘	σ^-	σ^+	⊘	σ^-	σ^+	⊘	σ^-	σ^+	⊘
$2p_+$	−K	σ^+	⊘	σ^-	σ^+	⊘	σ^-	σ^+	⊘	σ^-	σ^+	⊘
	K	σ^-	σ^+	⊘	σ^-	σ^+	⊘	σ^-	σ^+	⊘	σ^-	σ^+
$2p_-$	−K	σ^-	σ^+	⊘	σ^-	σ^+	⊘	σ^-	σ^+	⊘	σ^-	σ^+
	K	⊘	σ^-	σ^+	⊘	σ^-	σ^+	⊘	σ^-	σ^+	⊘	σ^-

those in the bulk. This is mainly due to nonlocal Coulomb screening in and out of the plane of the monolayer TMD. For example, the optical reflectance measurements in a typical ML TMD, WSe_2, show that the exciton series in these materials clearly deviate from the 2D hydrogen series [42]. The two-photon excitation spectroscopy combined with the many-body perturbation theory within the *GW* self-energy approximation and the Bethe-Salpeter equations also attest to the same [43]. However, these calculations also showed that there is a one-to-one correspondence between the exciton wave-function symmetry in ML TMDs and the 2D hydrogen model. By treating the exciton problem in ML TMDs as a 2D hydrogen model for the sake of exciton wave-function symmetry, we explore the higher-lying exciton states such as $2p_+$ and $2p_-$. The symmetries of $3d_\pm$ exciton states can be reduced to those of $2p_\mp$.

In Table V, we tabulated the optical selection rules for the bright A and B excitons of the $1s$ and $2p_\pm$ series in the dipole coupling regime. When the vortex beam has zero OAM ($l = 0$), it reduces to an ordinary Gaussian laser beam without a helical structure. Typically, in describing the general features of excitons formed with ordinary light beams, one can reasonably assume the electronic bands to be parabolic and axially symmetric. In this description, the transition rates are proportional to the square of the envelope function at the origin, which describes the relative motion of the electron-hole pair. For the first-class (or zeroth-order) transitions, only the *s*-like excitons have nonzero value at the origin. Therefore, typically, one does not observe *p*-like exciton signals in one-photon spectroscopy [25]. However, in the case of monolayer TMDs, the breaking of the axial symmetry in the ML crystal in terms of the discrete threefold rotation causes the bands (especially the valence bands) to develop trigonal warping [28,44], and the band dispersion can no longer be described using parabolic bands with an axial symmetry. Fundamentally, this symmetry breaking and its consequences are included in the band symmetry and its point group. Therefore, $2p$ excitonic states are allowed by symmetry because there is a mixing between $2s$ and $2p$ levels due to the trigonal warping [45]. The strength of the $2p$ excitons is expected to be two orders of magnitude weaker than that of $1s$ excitons [46]. In the same table, we can also observe that both A- and B-type bright excitons follow the same selection rules. The selection rules for the $2p_\pm$ excitons differ from those of the $1s$ excitons; nevertheless, the order of the light polarization with respect to the OAM stays the same—the pattern has the periodicity of three units of OAM.

TABLE VI. Dark A excitons in the quadrupole coupling regime: Optical selection rules for the *dark* A excitons created by laser beams carrying orbital angular momentum (OAM) and spin angular momentum (SAM) for $1s$ and $2p_\pm$ exciton envelope functions.

l (OAM)		−5	−4	−3	−2	−1	0	+1	+2	+3	+4	+5
$1s$	−K	σ^-	σ^+	⊘	σ^-	σ^+	⊘	σ^-	σ^+	⊘	σ^-	σ^+
	K	σ^-	σ^+	⊘	σ^-	σ^+	⊘	σ^-	σ^+	⊘	σ^-	σ^+
$2p_+$	−K	⊘	σ^-	σ^+	⊘	σ^-	σ^+	⊘	σ^-	σ^+	⊘	σ^-
	K	⊘	σ^-	σ^+	⊘	σ^-	σ^+	⊘	σ^-	σ^+	⊘	σ^-
$2p_-$	−K	σ^+	⊘	σ^-	σ^+	⊘	σ^-	σ^+	⊘	σ^-	σ^+	⊘
	K	σ^+	⊘	σ^-	σ^+	⊘	σ^-	σ^+	⊘	σ^-	σ^+	⊘

Because dark exciton states cannot be realized with circularly polarized light in the dipole coupling regime (see Table III), we only display the selection rules for dark excitons in the quadrupole regime in Tables VI and VII for the $1s$ and $2p_\pm$ series. It is possible to create dark excitons with vortex beams in the quadrupole coupling regime for various exciton states. Using an appropriate vortex beam, we can selectively excite $1s$ or $2p_\pm$ dark A (B) excitons. In Figs. 2 and 3, we pictorially show the allowed A and B dark exciton transitions from the crystal ground state to the $1s$, $2p_+$, and $2p_-$ exciton states for the vortex beam for a particular value of the light OAM ($l = 1$). According to the diagrams, the selection rules are the same in both valleys for the dark A excitons and differ for the dark B excitons.

IV. CONCLUSION

Using symmetry arguments, we have derived optical selection rules for the spin-forbidden dark excitons and bright excitons in a monolayer TMD crystal excited by a vortex beam. In the dipole coupling regime, creating A and B bright excitons follows the same selection rules in individual valleys. In addition to $1s$ excitons, we can also selectively create $2p_\pm$ excitons. In this work, we showed the necessary conditions for creating various dark excitons in terms of the optical selection rules. Specifically, the vortex beams can be used to create A and B dark excitons in the quadrupole coupling regime, and we provided the tables for optical selection rules for such transitions. This demonstrates the usefulness of the vortex

TABLE VII. Dark B excitons in the quadrupole coupling regime: Optical selection rules for the *dark* B-excitons created by laser beams carrying orbital angular momentum (OAM) and spin angular momentum (SAM) for $1s$ and $2p_\pm$ exciton envelope functions.

l (OAM)		−5	−4	−3	−2	−1	0	+1	+2	+3	+4	+5
$1s$	−K	σ^+	⊘	σ^-	σ^+	⊘	σ^-	σ^+	⊘	σ^-	σ^+	⊘
	K	⊘	σ^-	σ^+	⊘	σ^-	σ^+	⊘	σ^-	σ^+	⊘	σ^-
$2p_+$	−K	σ^-	σ^+	⊘	σ^-	σ^+	⊘	σ^-	σ^+	⊘	σ^-	σ^+
	K	σ^+	⊘	σ^-	σ^+	⊘	σ^-	σ^+	⊘	σ^-	σ^+	⊘
$2p_-$	−K	⊘	σ^-	σ^+	⊘	σ^-	σ^+	⊘	σ^-	σ^+	⊘	σ^-
	K	σ^-	σ^+	⊘	σ^-	σ^+	⊘	σ^-	σ^+	⊘	σ^-	σ^+

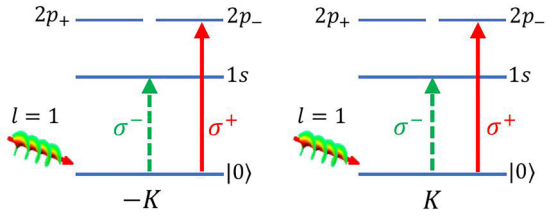

FIG. 2. Dark A excitons in the quadrupole coupling regime: The diagram describes the allowed transitions from the crystal ground state to the $1s$ and $2p_\pm$ exciton states for the dark B excitons when the vortex beam has $l = 1$ orbital angular momentum. The symmetries of all higher-lying exciton states can be reduced to the symmetries of these three states.

beams with a nonzero orbital angular momentum in generating otherwise forbidden dark excitons, which are long-lived and have long coherence times.

The selection rules presented in this work, however, have limitations. In addition to the relative motion of excitons considered in this work, vortex beams have also been recently observed to affect the center-of-mass motion of excitons in monolayer TMDs where the spectral energy peak [47], the valley dynamics [48], as well as the spin dynamics [49] of excitons were controlled by the OAM of a vortex beam. The unifying theme of these reports was the importance of the center-of-mass momentum of excitons in mediating the electron-hole exchange interaction, which brought about the observed phenomena. To generalize the selection rules for the finite center-of-mass momentum excitons, which can facilitate various scattering processes, including the electron-hole exchange interaction, one needs to adopt a more general theoretical framework, for example with an effective Hamiltonian based upon the solution of the Bethe-Salpeter equation [50,51].

Optically created quantum states such as these dark exciton states can be a useful tool in many quantum device applications. For example, this could be an efficient method of transduction between semiconductor spin qubits with great tunability for information processing and photonic qubits with a long coherence time to use for communications.

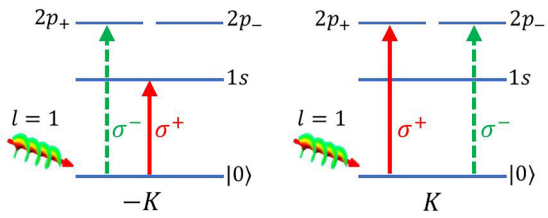

FIG. 3. Dark B excitons in the quadrupole coupling regime: The diagram describes the allowed transitions from the crystal ground state to the $1s$ and $2p_\pm$ exciton states for the dark B excitons when the vortex beam has $l = 1$ orbital angular momentum. The symmetries of all higher-lying exciton states can be reduced to the symmetries of these three states.

ACKNOWLEDGMENTS

This material is based upon work supported by the Air Force Office of Scientific Research under Award No. FA9550-23-1-0477. C.L. acknowledges financial support from the National Science Foundation via Grant No. NSF DMR-1827745.

APPENDIX: SYMMETRY ANALYSIS

1. Band symmetry

We label the electronic bands of our effective two-band (spin-split) model with their respective irreducible representations in the double-point group C_{3h} relevant at the $\pm K$ momentum points. To assign a specific irrep to the valence (conduction) band, we construct a tight-binding wave function by symmetry-adapted atomic orbitals with respect to the threefold rotation symmetry of the crystal. Applying the threefold rotation operator C_3 on this wave function gives an eigenvalue that can be used to read off their respective irreps from the character Table VIII.

According to the DFT band-structure calculations [28], the valence (conduction) bands at the $\pm K$ momentum points in the Brillouin zone of the ML TMD crystal are predominantly made of the $d_{x^2-y^2}$ and d_{xy} (d_{z^2}) atomic orbitals of the transition metal atoms. Using these atomic orbitals as the basis functions [9] that are symmetrized with respect to the threefold rotation operator C_3^+ relevant to the monolayer crystal symmetry, we can construct a tight-binding wave function [53]. For the valence (conduction) bands denoted by α index at the K momentum point of the reduced Brillouin zone, the wave function that satisfies the Bloch theorem is then given by

$$\psi_\alpha^K(\boldsymbol{r}) = \frac{1}{\sqrt{N}} \sum_n e^{i\boldsymbol{K}\cdot(\boldsymbol{R}_n+\boldsymbol{\zeta})} \phi_\alpha(\boldsymbol{r} - \boldsymbol{R}_n - \boldsymbol{\zeta}). \tag{A1}$$

Here, the summation is run over the lattice vectors $\boldsymbol{R}_n$, and $\boldsymbol{\zeta} = (\frac{1}{2}, \frac{1}{2\sqrt{3}})a$ is the position of the transition metal atom relative to the hexagon center h inside the unit cell [see Fig. 1(b)]. The momentum point $K = \frac{2\pi}{a}(\frac{2}{3}, 0)$ or the K valley is taken relative to the Brillouin zone center $\Gamma = (0, 0)$ [see Fig. 1(e)]. The valence band constructed from the atomic orbitals at this valley is $\phi_v(\boldsymbol{r}) \propto \frac{1}{\sqrt{2}}(d_{x^2-y^2} + id_{xy})$ and the same for the conduction band is $\phi_c(\boldsymbol{r}) \propto d_{z^2}$.

Thus, the eigenvalue of the operator C_3^+ has two components: one comes from the rotation of the atomic orbital around its own center by $2\pi/3$ degrees counterclockwise, and the other comes from the change of the Bloch phase after the threefold rotation. We note that the rotation operator affects the phase change differently depending on the rotation center. We took the hexagon center h to be the rotation center. One could also equally take the transition metal atom to be the rotation center. However, such a choice would alter the band irreps, but the selection rules would not change. By applying the C_3^+ on the valence band at the K valley $C_3^+\psi_v^K(\boldsymbol{r}) = \eta_c\psi_v^K(\boldsymbol{r})$, we obtain its eigenvalue $\eta_c = \mu_v\nu_v$, which has two components coming from the change in the Bloch phase μ_v and the rotation of the atomic orbital ν_v. In our case, we obtain $\mu_v = e^{-i\frac{2\pi}{3}}$. The atomic orbital for the valence band can be

TABLE VIII. Character table for the C_{3h} double-group [52]. Here, $\omega = \exp(i2\pi/3)$ and $\omega^* = \exp(-i2\pi/3)$.

C_{3h}	E	C_3^+	C_3^-	σ_h	S_3^+	S_3^-	$\bar{E}$	$\bar{C}_3^+$	$\bar{C}_3^-$	$\bar{\sigma}_h$	$\bar{S}_3^+$	$\bar{S}_3^-$	Bases
Γ_1	1	1	1	1	1	1	1	1	1	1	1	1	R
Γ_2	1	ω	ω^*	1	ω	ω^*	1	ω	ω^*	1	ω	ω^*	x+iy
Γ_3	1	ω^*	ω	1	ω^*	ω	1	ω^*	ω	1	ω^*	ω	x-iy
Γ_4	1	1	1	-1	-1	-1	1	1	1	-1	-1	-1	z
Γ_5	1	ω	ω^*	-1	$-\omega$	$-\omega^*$	1	ω	ω^*	-1	$-\omega$	$-\omega^*$	(x+iy)z
Γ_6	1	ω^*	ω	-1	$-\omega^*$	$-\omega$	1	ω^*	ω	-1	$-\omega^*$	$-\omega$	(x-iy)z
Γ_7	1	$-\omega$	$-\omega^*$	i	$-i\omega$	$i\omega^*$	-1	ω	ω^*	$-i$	$i\omega$	$-i\omega^*$	$\chi(1/2,+1/2)$
Γ_8	1	$-\omega^*$	$-\omega$	$-i$	$i\omega^*$	$-i\omega$	-1	ω^*	ω	i	$-i\omega^*$	$i\omega$	$\chi(1/2,-1/2)$
Γ_9	1	$-\omega$	$-\omega^*$	$-i$	$i\omega$	$-i\omega^*$	-1	ω	ω^*	i	$-i\omega$	$i\omega^*$	
Γ_{10}	1	$-\omega^*$	$-\omega$	i	$-i\omega^*$	$i\omega$	-1	ω^*	ω	$-i$	$i\omega^*$	$-i\omega$	
Γ_{11}	1	-1	-1	i	$-i$	i	-1	1	1	$-i$	i	$-i$	
Γ_{12}	1	-1	-1	$-i$	i	$-i$	-1	1	1	i	$-i$	i	

shown to be proportional to a spherical harmonic function as $\phi_v(\boldsymbol{r}) \propto Y_2^2(\boldsymbol{r})$ and $\nu_v = e^{+i\frac{2\pi}{3}}$. So the application of the C_3^+ operator on $Y_2^2(\boldsymbol{r})$ yields $\nu_v = e^{-i\frac{2\pi}{3}2} \equiv e^{+i\frac{2\pi}{3}}$. Consequently, the total eigenvalue $\eta_v = 1$. From the character Table VIII we see that this eigenvalue of the C_3^+ corresponds to the Γ_1 irrep for the valence band at the K valley without considering the spin-orbit interaction.

Similarly, we can follow the same procedure for the conduction band. The eigenvalue component coming from the Bloch phase change is the same in this case as well, $\mu_c = e^{-i\frac{2\pi}{3}}$. The atomic orbital for the conduction band is also proportional to a spherical harmonic function $\phi_c(\boldsymbol{r}) \propto Y_2^0(\boldsymbol{r})$. Therefore, the eigenvalue $\nu_c = e^{-i\frac{2\pi}{3}0} \equiv 1$. Consequently, the total eigenvalue $\eta_c = e^{-i\frac{2\pi}{3}}$. From the character Table VIII we see that this eigenvalue, on the other hand, corresponds to the Γ_3 irrep for the valence band at the K valley without considering the spin-orbit interaction.

Taking the spin-orbit splitting of the valence band into account [54] gives the following irreps for the spin-split valence bands: $\Gamma_1 \otimes \Gamma_7 = \Gamma_7$ and $\Gamma_1 \otimes \Gamma_8 = \Gamma_8$ (see Table IX). In this case, the spin-split band with a positive spin-orbit interaction energy lies higher in the band diagram [see Fig. 1(f)]. Similarly, we can also label the spin-split conduction bands with their respective irreps: $\Gamma_3 \otimes \Gamma_7 = \Gamma_{11}$, $\Gamma_3 \otimes \Gamma_8 = \Gamma_9$. The order of the spin-split conduction bands can be inferred from the first-principles band-structure calculations because the origin of the spin-orbit splitting in the conduction band is nontrivial and due to the competition between the minority orbitals coming from the chalcogen atom and the interaction with other nearby bands [28]. The irreps of the bands at the $-K$ valley are related to those of the bands at the K valley by the time-reversal symmetry.

TABLE IX. Multiplication table for the C_{3h} double-group [52].

	Γ_1	Γ_2	Γ_3	Γ_4	Γ_5	Γ_6	Γ_7	Γ_8	Γ_9	Γ_{10}	Γ_{11}	Γ_{12}
Γ_1	Γ_1	Γ_2	Γ_3	Γ_4	Γ_5	Γ_6	Γ_7	Γ_8	Γ_9	Γ_{10}	Γ_{11}	Γ_{12}
Γ_2	Γ_2	Γ_3	Γ_1	Γ_5	Γ_6	Γ_4	Γ_{10}	Γ_{12}	Γ_8	Γ_{11}	Γ_7	Γ_9
Γ_3	Γ_3	Γ_1	Γ_2	Γ_6	Γ_4	Γ_5	Γ_{11}	Γ_9	Γ_{12}	Γ_7	Γ_{10}	Γ_8
Γ_4	Γ_4	Γ_5	Γ_6	Γ_1	Γ_2	Γ_3	Γ_9	Γ_{10}	Γ_7	Γ_8	Γ_{12}	Γ_{11}
Γ_5	Γ_5	Γ_6	Γ_4	Γ_2	Γ_3	Γ_1	Γ_8	Γ_{11}	Γ_{10}	Γ_{12}	Γ_9	Γ_7
Γ_6	Γ_6	Γ_4	Γ_5	Γ_3	Γ_1	Γ_2	Γ_{12}	Γ_7	Γ_{11}	Γ_9	Γ_8	Γ_{10}
Γ_7	Γ_7	Γ_{10}	Γ_{11}	Γ_9	Γ_8	Γ_{12}	Γ_6	Γ_1	Γ_3	Γ_4	Γ_5	Γ_2
Γ_8	Γ_8	Γ_{12}	Γ_9	Γ_{10}	Γ_{11}	Γ_7	Γ_1	Γ_5	Γ_4	Γ_2	Γ_3	Γ_6
Γ_9	Γ_9	Γ_8	Γ_{12}	Γ_7	Γ_{10}	Γ_{11}	Γ_3	Γ_4	Γ_6	Γ_1	Γ_2	Γ_5
Γ_{10}	Γ_{10}	Γ_{11}	Γ_7	Γ_8	Γ_{12}	Γ_9	Γ_4	Γ_2	Γ_1	Γ_5	Γ_6	Γ_3
Γ_{11}	Γ_{11}	Γ_7	Γ_{10}	Γ_{12}	Γ_9	Γ_8	Γ_5	Γ_3	Γ_2	Γ_6	Γ_4	Γ_1
Γ_{12}	Γ_{12}	Γ_9	Γ_8	Γ_{11}	Γ_7	Γ_{10}	Γ_2	Γ_6	Γ_5	Γ_3	Γ_1	Γ_4

2. Vortex beam profile

During the analysis of the spatial profile of the beam, we make use of the cylindrical and spherical coordinates interchangeably. The vortex beam propagates along the z-axis, which is perpendicular to the ML TMD crystal lying on the xy plane [see Fig. 1(h)]. By placing a ML TMD crystal around the beam waist ($z \approx 0$), we can obtain a much simplified spatial profile for the fundamental radial mode ($p = 0$) of the Laguerre-Gauss beam where the complex Gouy phase vanishes. We limit our attention to the fundamental radial mode ($p = 0$) as p does not affect the selection rules qualitatively. In the vicinity of the beam vortex ($\rho \ll w_0$):

$$A^l(\rho, \phi, z) = \sqrt{\frac{2^{|l|+1}}{\pi |l|!}} \frac{\rho^{|l|}}{w_0^{|l|}} e^{il\phi}. \tag{A2}$$

In the spherical coordinates, the vortex beam assumes the following form:

$$\begin{aligned} A^l(r, \theta, \phi) &= \sqrt{\frac{2^{|l|+1}}{\pi |l|!}} \frac{r^{|l|}}{w_0^{|l|}} (\sin\theta)^{|l|} e^{il\phi} \\ &= (-1)^l \sqrt{\frac{2^{3|l|+3}|l|!}{(2|l|+1)!}} \frac{r^{|l|}}{w_0^{|l|}} Y_{|l|}^l, \end{aligned} \tag{A3}$$

TABLE X. Symmetry of the beam polarization (SAM).

SAM	Bases	Irreps
σ^-	$Y_1^{-1}(\theta,\phi) = \frac{1}{2}\sqrt{\frac{3}{2\pi}}\frac{x-iy}{r}$	Γ_3
π	$Y_1^0(\theta,\phi) = \frac{1}{2}\sqrt{\frac{3}{\pi}}\frac{z}{r}$	Γ_4
σ^+	$Y_1^{+1}(\theta,\phi) = -\frac{1}{2}\sqrt{\frac{3}{2\pi}}\frac{x+iy}{r}$	Γ_2

TABLE XI. Symmetry of the beam OAM for $l \leqslant 2$.

OAM	Bases	Irreps
-2	$Y_2^{-2}(\theta,\phi) = \frac{1}{4}\sqrt{\frac{15}{2\pi}}\frac{(x-iy)^2}{r^2}$	Γ_2
-1	$Y_1^{-1}(\theta,\phi) = \frac{1}{2}\sqrt{\frac{3}{2\pi}}\frac{x-iy}{r}$	Γ_3
0	$Y_0^0(\theta,\phi) = \frac{1}{2}\sqrt{\frac{1}{\pi}}$	Γ_1
$+1$	$Y_1^{+1}(\theta,\phi) = -\frac{1}{2}\sqrt{\frac{3}{2\pi}}\frac{x+iy}{r}$	Γ_2
$+2$	$Y_2^{+2}(\theta,\phi) = \frac{1}{4}\sqrt{\frac{15}{2\pi}}\frac{(x+iy)^2}{r^2}$	Γ_3

where we have used the identity $(\sin\theta)^{|l|}e^{il\phi} = (-1)^l 2^{|l|}|l|!\sqrt{4\pi/(2|l|+1)!}Y^l_{|l|}$. Here, $Y^l_{|l|}$ is a spherical harmonic function of degree (order) $|l|$ (l). The transformation symmetry properties of the SAM and OAM of the light are given in Tables X and XI, respectively.

3. Transition matrix element

Fermi's Golden rule states that a direct optical transition rate from the crystal ground state to the excited state is given by

$$R = \frac{2\pi}{\hbar}\sum_X |\langle\Psi_X|\hat{H}_{\rm int}|0\rangle|^2\delta(E_X - E_0 - \hbar\omega), \quad \text{(A4)}$$

where $\hat{H}_{\rm int}$ is the light-crystal interaction Hamiltonian and ω is the light frequency. The sum is taken over all final (exciton) states. We assume that the linear center-of-mass momentum of excitons is only determined by the in-plane momentum of the light beam, which is negligible for normal incidence [55]. Nevertheless, we do not rule out the possibility of the transition rates being affected by the finite center-of-mass momentum of excitons, which would require a more general framework [50]. In this approximation, the exciton wave function is a triple product of the electron-hole envelope function, and the electron and hole Bloch wave functions at the conduction and valence bands, respectively [56],

$$\Psi_X(\boldsymbol{r}_e,\boldsymbol{r}_h) = \sum_{\boldsymbol{k}} F_{nm}(\boldsymbol{k})\psi_{c\boldsymbol{k}}(\boldsymbol{r}_e)\psi^*_{v\boldsymbol{k}}(\boldsymbol{r}_h), \quad \text{(A5)}$$

where $F_{nm}(\boldsymbol{k}) = R_{n|m|}(k)e^{im\phi}$ is the Fourier transform of the 2D exciton envelope function $\Phi_{nm}(\boldsymbol{r})$. Because of the spherical symmetry of the radial function both in real and reciprocal space, the phase factor entirely defines the symmetry of the exciton envelope function. Because $\exp(im\phi) \propto [x + \mathrm{sgn}(m)iy]^{|m|}$ in Cartesian coordinates, it can serve as the bases

TABLE XII. Basis functions and corresponding irreps of few exciton envelope functions.

Envelope func.	Bases	Irreps
$1s$	1	Γ_1
$2p_+$	$(x+iy)$	Γ_2
$2p_-$	$(x\text{-}iy)$	Γ_3
$3d_+$	$(x+iy)^2$	Γ_3
$3d_-$	$(x-iy)^2$	Γ_2

TABLE XIII. Symmetry of $1s$ envelope function, conduction band, valence band, and exciton wave functions.

Type	Valley	Envelope	Conduction	Valence	Exciton
Bright A	$-K$	Γ_1	Γ_{12}	Γ_8	Γ_2
	$+K$	Γ_1	Γ_{11}	Γ_7	Γ_3
Bright B	$-K$	Γ_1	Γ_{10}	Γ_7	Γ_2
	$+K$	Γ_1	Γ_9	Γ_8	Γ_3
Dark A	$-K$	Γ_1	Γ_{10}	Γ_8	Γ_4
	$+K$	Γ_1	Γ_9	Γ_7	Γ_4
Dark B	$-K$	Γ_1	Γ_{12}	Γ_7	Γ_6
	$+K$	Γ_1	Γ_{11}	Γ_8	Γ_5

for the irreducible representations of the group relevant at individual valleys. Subsequently, one can assign an irreducible representation to each exciton state in the series depending upon the sign and value of m (see Table XII). For $m = 0$ (i.e., $1s$ exciton), the irreducible representation of the envelope function is Γ_1, while for $m = \pm 1$, it is Γ_2 and Γ_3, respectively. For $|m| > 1$, it will be $|m|$ direct products of Γ_2 or Γ_3. Therefore, the triple direct product represents the symmetry of an exciton state

$$\Gamma_X = \Gamma_{\rm env} \otimes \Gamma_c \otimes \Gamma^*_v. \quad \text{(A6)}$$

In the Coulomb gauge, one can show that the interaction Hamiltonian

$$\hat{H}_{\rm int} \propto e^{ikz}\boldsymbol{r}\cdot\boldsymbol{\epsilon}A^l \approx (-1)^l\sqrt{\frac{2^{3|l|+3}|l|!}{(2|l|+1)!}}\frac{r^{|l|+1}}{w_0^{|l|}}(1+ikz)Y^s_1Y^l_{|l|}. \quad \text{(A7)}$$

Here, the spherical harmonic function $Y^l_{|l|}$ (Y^s_1) expresses the orbital (spin) angular momentum of light. The right (left) circularly polarized light is designated with $s = +1(-1)$ values. When the light beam is polarized along the direction perpendicular to the crystal plane, $s = 0$. As these functions form bases for the irreps in the double-point group C_{3h} relevant at the $\pm K$ valleys, we can assign corresponding irreps depending on the values of l and s. The symmetry properties of the spin degree of freedom are represented by Γ_2 (Γ_3) for $s = +1$ (-1) and Γ_4 for $s = 0$ since $Y_1^{\pm 1} \propto (x \pm iy)$ and $Y_1^0 \propto z$, respectively. These transformation properties of SAM

TABLE XIV. Total symmetry of a vortex beam with OAM of $|l| \leqslant 1$ in the dipole and quadrupole regimes.

OAM	SAM	Dipole	Quadrupole
-1	σ^-	Γ_2	Γ_5
	π	Γ_6	Γ_3
	σ^+	Γ_1	Γ_4
0	σ^-	Γ_3	Γ_6
	π	Γ_4	Γ_1
	σ^+	Γ_2	Γ_5
$+1$	σ^-	Γ_1	Γ_4
	π	Γ_5	Γ_2
	σ^+	Γ_3	Γ_6

are tabulated in Table X. On the other hand, for the spherical harmonic function $Y^l_{|l|} \propto [x + \mathrm{sgn}(l)iy]^{|l|}$, we can assign an irrep for specific values of the beam OAM l. For example, for $l = 1$ (-1) it is Γ_2 (Γ_3) and for $l = 0$ it is Γ_1. For high values of l one needs to compute a direct product of l number of Γ_2 or Γ_3 using the irrep multiplication table for the double-group of C_{3h}. These transformation properties of the vortex beam for a few values of OAM are tabulated in Table XI. When the vector potential is expanded in powers of kz (i.e., $e^{ikz} = 1 + ikz + \cdots$), its order has the symmetry of Γ_1 for the zeroth-order transition (electric dipole) and Γ_4 for the first-order transition (electric quadrupole plus magnetic dipole). We note that the prefactors that are not dependent on the orbital coordinates (x, y, z) do not affect the symmetry transformations because they constitute a basis to the totally symmetric irrep of the group, Γ_1. Consequently, the symmetry of the vortex beam is equal to

$$\Gamma_{\mathrm{beam}} = \Gamma_{\mathrm{order}} \otimes \Gamma_{\mathrm{OAM}} \otimes \Gamma_{\mathrm{SAM}}. \tag{A8}$$

For an optical transition from the crystal ground state to an excitonic state to occur, the transition matrix element $\langle \Psi_X | \hat{H}_{\mathrm{int}} | 0 \rangle$ must be nonzero (see Eq. (A4)). For that to happen, the triple direct product of the exciton state, vortex beam, and the crystal ground state must span the totally symmetric irrep of the group C_{3h}, which is Γ_1. The symmetry of the crystal ground state is also represented by Γ_1. Thus, the allowed exciton transitions satisfy the following direct product equation:

$$\Gamma^*_X \otimes \Gamma_{\mathrm{beam}} \otimes \Gamma_1 = \Gamma_1. \tag{A9}$$

This statement is also known as the matrix element theorem [25,57], which states that the symmetry of the final (exciton) state must contain symmetry of the driving field operator for an excitation from the ground state to occur.

In Table XIII, we tabulate the symmetry of the $1s$ bright (and dark) exciton of A (and B) type. For the formation of a particular type of exciton by a vortex beam, its total symmetry (Table XIV) should match that of the exciton [Eq. (A9)]. By comparing the symmetry of a vortex beam and that of a $1s$ exciton of a given type, one can obtain the allowed transitions. For example, in the dipole coupling regime, an ordinary Gaussian beam of light ($l = 0$) with σ^- (σ^+) polarization can create a bright exciton only at K ($-K$) valley. These are the famous valley selection rules for ML TMDs [12].

[1] E. Poem, Y. Kodriano, C. Tradonsky, N. H. Lindner, B. D. Gerardot, P. M. Petroff, and D. Gershoni, Accessing the dark exciton with light, Nat. Phys. **6**, 993 (2010).

[2] I. Schwartz, E. R. Schmidgall, L. Gantz, D. Cogan, E. Bordo, Y. Don, M. Zielinski, and D. Gershoni, Deterministic Writing and Control of the Dark Exciton Spin Using Single Short Optical Pulses, Phys. Rev. X **5**, 011009 (2015).

[3] J. Madéo, M. K. L. Man, C. Sahoo, M. Campbell, V. Pareek, E. L. Wong, A. Al-Mahboob, N. S. Chan, A. Karmakar, B. M. K. Mariserla, X. Li, T. F. Heinz, T. Cao, and K. M. Dani, Directly visualizing the momentum-forbidden dark excitons and their dynamics in atomically thin semiconductors, Science **370**, 1199 (2020).

[4] A. Rustagi and A. F. Kemper, Photoemission signature of excitons, Phys. Rev. B **97**, 235310 (2018).

[5] G. Wang, A. Chernikov, M. M. Glazov, T. F. Heinz, X. Marie, T. Amand, and B. Urbaszek, Colloquium: Excitons in atomically thin transition metal dichalcogenides, Rev. Mod. Phys. **90**, 021001 (2018).

[6] K. S. Novoselov, D. Jiang, F. Schedin, T. J. Booth, V. V. Khotkevich, S. V. Morozov, and A. K. Geim, Two-dimensional atomic crystals, Proc. Natl. Acad. Sci. (USA) **102**, 10451 (2005).

[7] K. F. Mak, C. Lee, J. Hone, J. Shan, and T. F. Heinz, Atomically Thin MoS_2: A New Direct-Gap Semiconductor, Phys. Rev. Lett. **105**, 136805 (2010).

[8] A. Splendiani, L. Sun, Y. Zhang, T. Li, J. Kim, C.-Y. Chim, G. Galli, and F. Wang, Emerging photoluminescence in monolayer mos_2, Nano Lett. **10**, 1271 (2010).

[9] D. Xiao, G.-B. Liu, W. Feng, X. Xu, and W. Yao, Coupled Spin and Valley Physics in Monolayers of MoS_2 and Other Group-VI Dichalcogenides, Phys. Rev. Lett. **108**, 196802 (2012).

[10] T. Cao, G. Wang, W. Han, H. Ye, C. Zhu, J. Shi, Q. Niu, P. Tan, E. Wang, B. Liu, and J. Feng, Valley-selective circular dichroism of monolayer molybdenum disulphide, Nat. Commun. **3**, 887 (2012).

[11] K. F. Mak, K. He, J. Shan, and T. F. Heinz, Control of valley polarization in monolayer MoS_2 by optical helicity, Nat. Nanotechnol. **7**, 494 (2012).

[12] H. Zeng, J. Dai, W. Yao, D. Xiao, and X. Cui, Valley polarization in MoS_2 monolayers by optical pumping, Nat. Nanotechnol. **7**, 490 (2012).

[13] X.-X. Zhang, T. Cao, Z. Lu, Y.-C. Lin, F. Zhang, Y. Wang, Z. Li, J. C. Hone, J. A. Robinson, D. Smirnov, S. G. Louie, and T. F. Heinz, Magnetic brightening and control of dark excitons in monolayer WSe_2, Nat. Nanotechnol. **12**, 883 (2017).

[14] Y. Zhou, G. Scuri, D. S. Wild, A. A. High, A. Dibos, L. A. Jauregui, C. Shu, K. D. Greve, K. Pistunova, A. Y. Joe, T. Taniguchi, K. Watanabe, P. Kim, M. D. Lukin, and H. Park, Probing dark excitons in atomically thin semiconductors via near-field coupling to surface plasmon polaritons, Nat. Nanotechnol. **12**, 856 (2017).

[15] R. A. Beth, Mechanical detection and measurement of the angular momentum of light, Phys. Rev. **50**, 115 (1936).

[16] L. Allen, M. W. Beijersbergen, R. J. C. Spreeuw, and J. P. Woerdman, Orbital angular momentum of light and the transformation of Laguerre-Gaussian laser modes, Phys. Rev. A **45**, 8185 (1992).

[17] G. F. Quinteiro Rosen, P. I. Tamborenea, and T. Kuhn, Interplay between optical vortices and condensed matter, Rev. Mod. Phys. **94**, 035003 (2022).

[18] A. M. Konzelmann, S. O. Krüger, and H. Giessen, Interaction of orbital angular momentum light with Rydberg excitons: Modifying dipole selection rules, Phys. Rev. B **100**, 115308 (2019).

[19] M. E. J. Friese, T. A. Nieminen, N. R. Heckenberg, and H. Rubinsztein-Dunlop, Optical alignment and spinning of laser-trapped microscopic particles, Nature (London) **394**, 348 (1998).

[20] A. Picón, A. Benseny, J. Mompart, J. R. V. de Aldana, L. Plaja, G. F. Calvo, and L. Roso, Transferring orbital and spin angular momenta of light to atoms, New J. Phys. **12**, 083053 (2010).

[21] C. T. Schmiegelow, J. Schulz, H. Kaufmann, T. Ruster, U. G. Poschinger, and F. Schmidt-Kaler, Transfer of optical orbital angular momentum to a bound electron, Nat. Commun. **7**, 12998 (2016).

[22] J. D. Rodrigues, L. G. Marcassa, and J. T. Mendonça, Excitation of high orbital angular momentum Rydberg states with Laguerre–gauss beams, J. Phys. B **49**, 074007 (2016).

[23] R. Fickler, G. Campbell, B. Buchler, P. K. Lam, and A. Zeilinger, Quantum entanglement of angular momentum states with quantum numbers up to 10,010, Proc. Natl. Acad. Sci. (USA) **113**, 13642 (2016).

[24] G.-B. Liu, H. Pang, Y. Yao, and W. Yao, Intervalley coupling by quantum dot confinement potentials in monolayer transition metal dichalcogenides, New J. Phys. **16**, 105011 (2014).

[25] P. Y. Yu and M. Cardona, *Fundamentals of Semiconductors* (Springer, Berlin, 2010).

[26] G. Wang, C. Robert, M. M. Glazov, F. Cadiz, E. Courtade, T. Amand, D. Lagarde, T. Taniguchi, K. Watanabe, B. Urbaszek, and X. Marie, In-Plane Propagation of Light in Transition Metal Dichalcogenide Monolayers: Optical Selection Rules, Phys. Rev. Lett. **119**, 047401 (2017).

[27] C. Robert, T. Amand, F. Cadiz, D. Lagarde, E. Courtade, M. Manca, T. Taniguchi, K. Watanabe, B. Urbaszek, and X. Marie, Fine structure and lifetime of dark excitons in transition metal dichalcogenide monolayers, Phys. Rev. B **96**, 155423 (2017).

[28] A. Kormányos, G. Burkard, M. Gmitra, J. Fabian, V. Zólyomi, N. D. Drummond, and V. Fal'ko, $k \cdot p$ theory for two-dimensional transition metal dichalcogenide semiconductors, 2D Mater. **2**, 022001 (2015).

[29] H. Kogelnik and T. Li, Laser beams and resonators, Proc. IEEE Inst. Electr. Electron. Eng. **54**, 1312 (1966).

[30] K. Y. Bliokh and F. Nori, Transverse and longitudinal angular momenta of light, Phys. Rep. **592**, 1 (2015).

[31] M. Lax, W. H. Louisell, and W. B. McKnight, From maxwell to paraxial wave optics, Phys. Rev. A **11**, 1365 (1975).

[32] G. F. Quinteiro, F. Schmidt-Kaler, and C. T. Schmiegelow, Twisted-Light–Ion Interaction: The Role of Longitudinal Fields, Phys. Rev. Lett. **119**, 253203 (2017).

[33] J. P. Echeverry, B. Urbaszek, T. Amand, X. Marie, and I. C. Gerber, Splitting between bright and dark excitons in transition metal dichalcogenide monolayers, Phys. Rev. B **93**, 121107(R) (2016).

[34] T. Olsen, S. Latini, F. Rasmussen, and K. S. Thygesen, Simple Screened Hydrogen Model of Excitons in Two-Dimensional Materials, Phys. Rev. Lett. **116**, 056401 (2016).

[35] M. Shinada and S. Sugano, Interband optical transitions in extremely anisotropic semiconductors. I. Bound and unbound exciton absorption, J. Phys. Soc. Jpn. **21**, 1936 (1966).

[36] X. L. Yang, S. H. Guo, F. T. Chan, K. W. Wong, and W. Y. Ching, Analytic solution of a two-dimensional hydrogen atom. I. Nonrelativistic theory, Phys. Rev. A **43**, 1186 (1991).

[37] J.-Z. Zhang and J.-Z. Ma, Two-dimensional excitons in monolayer transition metal dichalcogenides from radial equation and variational calculations, J. Phys.: Condens. Matter **31**, 105702 (2019).

[38] D. Y. Qiu, F. H. da Jornada, and S. G. Louie, Optical Spectrum of MoS_2: Many-Body Effects and Diversity of Exciton States, Phys. Rev. Lett. **111**, 216805 (2013).

[39] V. E. Lembessis and M. Babiker, Enhanced Quadrupole Effects for Atoms in Optical Vortices, Phys. Rev. Lett. **110**, 083002 (2013).

[40] C. Schmiegelow and F. Schmidt-Kaler, Light with orbital angular momentum interacting with trapped ions, Eur. Phys. J. D **66**, 157 (2012).

[41] S. Ishii, N. Yokoshi, and H. Ishihara, Optical selection rule of monolayer transition metal dichalcogenide by an optical vortex, J. Phys.: Conf. Ser. **1220**, 012056 (2019).

[42] A. Chernikov, T. C. Berkelbach, H. M. Hill, A. Rigosi, Y. Li, B. Aslan, D. R. Reichman, M. S. Hybertsen, and T. F. Heinz, Exciton Binding Energy and Nonhydrogenic Rydberg series in Monolayer WS_2, Phys. Rev. Lett. **113**, 076802 (2014).

[43] Z. Ye, T. Cao, K. O'Brien, H. Zhu, X. Yin, Y. Wang, S. G. Louie, and X. Zhang, Probing excitonic dark states in single-layer tungsten disulphide, Nature (London) **513**, 214 (2014).

[44] H. Rostami, A. G. Moghaddam, and R. Asgari, Effective lattice hamiltonian for monolayer MoS_2: Tailoring electronic structure with perpendicular electric and magnetic fields, Phys. Rev. B **88**, 085440 (2013).

[45] M. M. Glazov, L. E. Golub, G. Wang, X. Marie, T. Amand, and B. Urbaszek, Intrinsic exciton-state mixing and nonlinear optical properties in transition metal dichalcogenide monolayers, Phys. Rev. B **95**, 035311 (2017).

[46] P. Gong, H. Yu, Y. Wang, and W. Yao, Optical selection rules for excitonic Rydberg series in the massive Dirac cones of hexagonal two-dimensional materials, Phys. Rev. B **95**, 125420 (2017).

[47] K. B. Simbulan, T.-D. Huang, G.-H. Peng, F. Li, O. J. Gomez Sanchez, J.-D. Lin, C.-I. Lu, C.-S. Yang, J. Qi, S.-J. Cheng, T.-H. Lu, and Y.-W. Lan, Selective photoexcitation of finite-momentum excitons in monolayer MoS_2 by twisted light, ACS Nano **15**, 3481 (2021).

[48] A. K. Pattanayak, P. Das, A. Dhara, D. Chakrabarty, S. Paul, K. Gurnani, M. M. Brundavanam, and S. Dhara, A steady-state approach for studying valley relaxation using an optical vortex beam, Nano Lett. **22**, 4712 (2022).

[49] A. K. Pattanayak, P. Das, D. Chakrabarty, A. Dhara, S. Paul, S. Maji, M. M. Brundavanam, and S. Dhara, Probing spin dynamics of 2d excitons with twisted light, ACS Photon. **9**, 3351 (2022).

[50] G.-H. Peng, O. J. G. Sanchez, W.-H. Li, P.-Y. Lo, and S.-J. Cheng, Tailoring the superposition of finite-momentum valley exciton states in transition-metal dichalcogenide monolayers by using polarized twisted light, Phys. Rev. B **106**, 155304 (2022).

[51] D. Y. Qiu, T. Cao, and S. G. Louie, Nonanalyticity, Valley Quantum Phases, and Lightlike Exciton Dispersion in Monolayer Transition Metal Dichalcogenides: Theory and First-Principles Calculations, Phys. Rev. Lett. **115**, 176801 (2015).

[52] G. Koster, J. Dimmock, R. Wheeler, and H. Statz, *Properties of the Thirty-two Point Groups*, M.I.T. Press Research Monographs (MIT Press, Cambridge, MA, 1963).

[53] N. W. Ashcroft and N. Mermin, *Solid State Physics* (Brooks/Cole, Florence, KY, 1976).

[54] M. S. Dresselhaus, G. Dresselhaus, and A. Jorio, *Group Theory*, 2008th ed. (Springer, Berlin, Germany, 2007).

[55] T. Graß, U. Bhattacharya, J. Sell, and M. Hafezi, Two-dimensional excitons from twisted light and the fate of the photon's orbital angular momentum, Phys. Rev. B **105**, 205202 (2022).

[56] R. J. Elliott, Intensity of optical absorption by excitons, Phys. Rev. **108**, 1384 (1957).

[57] J. Hopfdeld, Fine structure in the optical absorption edge of anisotropic crystals, J. Phys. Chem. Solids **15**, 97 (1960).